www.rericjournal.ait.ac.th

Reduced-Order Physics Modeling and Power Performance Analysis of Direct Methanol Fuel Cells

Phuoc Thanh Nguyen* and Thanh-Tuan Pham*[1]

ARTICLE INFO

Article history:
Received 17 January 2025
Received in revised form
10 May 2026
Accepted 11 June 2026

Keywords:
Direct Methanol Fuel Cell (DMFC)
Electrochemical modeling
Fuel cell performance analysis
Reduced-Order Modeling (ROM)
Passive Cell Dynamics

ABSTRACT

Direct methanol fuel cells (DMFCs) are attractive for portable, low-power applications because liquid methanol enables compact fuel storage and a simplified, potentially passive balance-of-plant. Performance is constrained by sluggish methanol oxidation kinetics, membrane/contact ohmic losses, and mass-transport limitations in porous layers. We develop a physics-based one-dimensional reduced-order model (ROM) to rapidly predict polarization and power with explicit voltage-loss decomposition. Cell voltage is written as the reversible potential evaluated at bulk/channel reference states minus additive activation, ohmic, and transport-induced concentration losses; the concentration term represents the bulk-to-interface Nernst shift under a no-double-counting convention. A lumped thermal transient submodel enables load-dependent temperature screening. The model uses effective single-phase transport closures with well-mixed bulk/channel reference states. Methanol crossover, cathodic mixed-potential losses, liquid-water flooding, and resolved multiphase transport are not included. Therefore, the reported efficiency and high-current predictions represent gross reduced-order estimates within the stated model scope. The ROM reproduces a bell-shaped power–current-density curve with a peak power density of 207 W/m² at i = 1563 A/m². At a practical point near 75% of peak power density, it predicts V = 0.2361 V, i = 679.6 A/m², and P = 160.5 W/m², corresponding to 20% efficiency. Loss analysis indicates activation losses dominate most conditions, whereas mid-load operation provides a balanced trade-off among power, efficiency, and thermal safety. The framework is computationally efficient, enabling rapid parametric studies and design screening.

1. INTRODUCTION

Due to the convenience of storing and delivering liquid fuel, alongside the ability to utilize a simplified, passive balance-of-plant, direct methanol fuel cells (DMFCs) have emerged as highly promising power solutions for portable devices. However, their actual efficiency is hindered by a combination of interrelated phenomena. Chief among these are the inherently slow kinetics of the anodic methanol oxidation reaction (MOR) and the significant ohmic resistance stemming from the polymer electrolyte and interfacial contacts. Furthermore, mass transport is frequently restricted within the porous media (GDL and CL), where excessive water buildup can severely obstruct oxygen diffusion. Finally, the permeation of unreacted methanol through the membrane to the cathode side triggers parasitic reactions, establishing mixed potentials that ultimately degrade the overall cell voltage and performance. Experimentally, methanol concentration has been shown to strongly affect the polarization characteristics and power output of passive DMFCs [1]. This effect is not purely a fuel-availability effect: higher methanol concentration can improve high-current performance by increasing methanol transport and operating temperature, but it also intensifies methanol crossover, lowers OCV, and reduces fuel/energy efficiency [2] [3].

Modeling studies have further suggested that coupled through-plane heat and species transport across the membrane–electrode assembly (MEA) can significantly influence polarization behavior and transport trends, especially for passive cells where the thermal balance is load dependent [4] [5]. From a transport perspective, water management and flooding remain important bottlenecks at medium-to-high current densities; combined experimental and modeling investigations have clarified water transport mechanisms and flooding conditions in DMFCs [6]. Diffusion-layer compression also introduces a practical trade-off: higher compression can improve electrical contact but reduce porosity and hinder transport, implying an operating-condition-dependent optimum compression ratio [7].

DOI: https://doi.org/10.64289/iej.26.0309.4929469

*Faculty of Energy Engineering and Transport, Ho Chi Minh City University of Technology and Engineering – HCM-UTE, Ho Chi Minh, Viet Nam.

[1]Corresponding author:
Email: tuanpt@hcmute.edu.vn

This trade-off is consistent with the broader role of the GDL/MPL structure, which supports the catalyst layer, collects current, redistributes reactants/products, and controls gas/liquid management; therefore, changes in GDL architecture or compression can simultaneously affect ohmic resistance, oxygen access, water removal, and methanol/CO_2 transport [8] [9]. In addition, explicitly resolved two-phase simulations show that CO_2 bubbles and liquid accumulation can obstruct local channel-scale transport, indicating that multiphase-resolved tools are more appropriate when bubble blockage, flooding, or local saturation behavior is the main focus [10].

On the modeling side, detailed steady-state one-dimensional (1D) two-phase frameworks have been developed to describe species transport and multiphase phenomena in porous layers for parametric studies [2]. Simulation–experiment comparisons, including current-density, show that 1D models can reproduce key trends when input parameters are selected consistently [11]. Furthermore, multilayer electrode designs (e.g., microporous layers) have been modeled and experimentally validated to quantify their roles in water/methanol transport and crossover mitigation [12]. At the system level, spatially resolved models coupled with system models have been used for operational optimization under varying loads [13], while transient studies with fluctuating methanol feed concentration suggest that electro-thermal dynamics can influence efficiency and stability [14]. Classical polymer electrolyte fuel cell modeling frameworks are also widely adopted to ensure physical interpretability and parameter-calibration capability [15].

Despite recent advances, there remains practical interest in models that are computationally efficient yet physically interpretable. For rapid design screening and control-oriented studies, it is crucial to predict *V-i* and *P-i* characteristics without resolving complex multiphase fields, to decompose voltage losses explicitly (separating kinetic, ohmic, and transport effects), and to estimate load-dependent temperature changes using a minimal transient formulation.

Rather than replacing detailed multiphase models, such lightweight formulations complement them. Since simplified DMFC models are already well established [4], [5], [11], [14], the contribution of this work is not mere dimensional reduction. Instead, the proposed ROM introduces an internally consistent voltage-loss budgeting framework that strictly avoids double-counting. By integrating bulk reference-state reversible potentials, Nernst-shift concentration losses, and lumped thermal screening, the framework evaluates *V-i* and *P-i* responses alongside activation, membrane/electrolyte ohmic losses, and reactant-demand metrics—rather than serving simply as fitted polarization curves. Practically, this approach is invaluable for the early-stage engineering design of portable, low-power DMFC systems constrained by fuel supply, passive heat rejection, and compactness. The framework effectively guides preliminary sizing and diagnostics before advancing to detailed multiphase simulations or physical prototyping.

In this paper, we propose a physics-based 1D reduced-order model (ROM) for passive DMFCs. Cell voltage is defined as the reversible potential at bulk/channel reference states minus effective activation, ohmic, and transport-induced concentration losses, enabling direct loss decomposition versus current density without double-counting. Coupled with a one-way lumped thermal transient submodel to assess load-dependent temperature rises, the ROM is validated against experimental polarization data using quantified errors (MAE/RMSE) and a representative loss budget. Here, "reduced-order" refers to a computationally efficient, physics-based 1D formulation using lumped, interpretable closures to capture key electrochemical and transport phenomena, bypassing the high costs of fully resolved multiphase modeling.

2. METHODOLOGY

2.1 DMFC structure, states, and modeling assumptions

Structurally, a direct methanol fuel cell (DMFC) is built around a central proton-exchange membrane (PEM). This membrane is sandwiched between the anodic and cathodic compartments, with each side comprising a reactive catalyst layer (CL), a porous diffusion medium, and a reactant flow channel. The present physics-based reduced-order model is formulated in one through-plane dimension across the membrane–electrode assembly (MEA) (Figure 1).

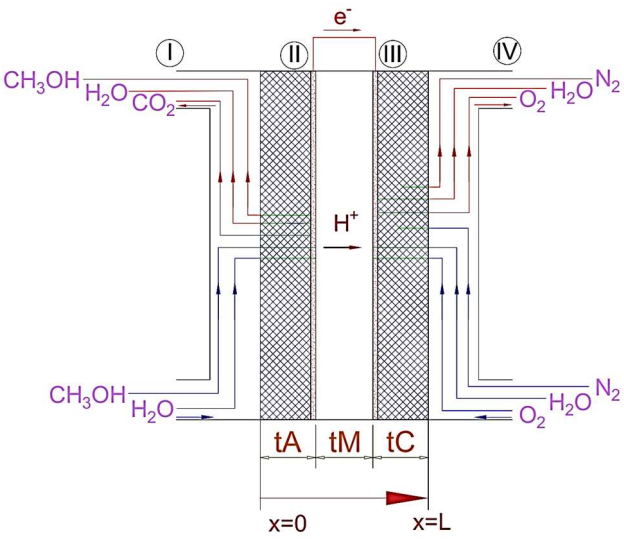

Fig. 1. 1D through-plane DMFC schematic with bulk/channel and interfacial states.

Four states are introduced to distinguish bulk/channel conditions from reaction-side conditions: state I (anode bulk/channel), state II (anode reaction side at the CL interface), state III (cathode reaction side at the CL interface), and state IV (cathode bulk/channel). In the channel and porous gas domains, the availability of gaseous species (e.g., O_2, CO_2, and water vapor) is represented by mole fractions X_k^s and the corresponding partial pressures are evaluated using Eq. (8) under the ideal-gas assumption. Methanol is supplied to the anode

as an aqueous species; therefore, its availability is represented using an effective concentration/activity parameter rather than a gas-phase partial pressure.

To keep the formulation compact and consistent with the implementation, the following assumptions are adopted: (i) transport is resolved only through-plane; axial variations along channels are embedded through boundary conditions and effective parameters; (ii) channels are treated as well-mixed bulk states (I, IV), while diffusion across porous layers is retained; (iii) catalyst layers are treated as negligibly thin reactive interfaces (states II and III); (iv) membrane protonic resistance dominates the ohmic loss, while remaining electronic/contact losses are lumped into effective parameters; and (v) single-phase transport is assumed, with water treated as vapor in the gas phase and as bound water in the PEM, while free liquid water is not modeled. Consequently, two-phase effects such as flooding are neglected and may mainly impact the very high-current regime.

The present ROM is designed for rapid parametric screening and diagnostic loss budgeting. While two-phase liquid-water phenomena are not explicitly resolved instead lumped into effective transport parameters-the model provides high fidelity within the activation and ohmic-dominated regimes. Consequently, predictions in the mass-transport-limited or flooding-dominated regimes should be interpreted as idealized upper bounds. Single-phase here refers to no explicit liquid-water phase and no multiphase fields in porous media; gas-domain species are treated as ideal gases, whereas methanol is an aqueous feed and is represented via an effective concentration/activity. Methanol crossover and the associated mixed-potential losses are not explicitly resolved; therefore, the reported efficiency and loss decomposition should be interpreted as gross (no-crossover) estimates within the reduced-order scope.

2.2 Cell reactions and reversible potential at bulk states

The overall DMFC reaction is:

$$CH_3OH + \frac{3}{2}O_2 \rightarrow 2H_2O + CO_2 \quad (1)$$

The anode and cathode half-reactions are written as follows.
Anode:

$$CH_3OH + H_2O \rightarrow 6H^+ + CO_2 + 6e^- \quad (2)$$

Cathode::

$$6H^+ + 6e^- + \frac{3}{2}O_2 \rightarrow 3H_2O \quad (3)$$

Based on Faraday's law of electrolysis and the stoichiometric coefficients, the molar fluxes (n) of the participating species are coupled to the current density (i) as follows:

$$\frac{i}{6F} = \frac{nH^+}{6} = n^A_{CH_3OH} = n^A_{CO_2} = \frac{2}{3}n^C_{O_2} = \frac{n^A_{H_2O}}{\gamma+1} = \frac{n^{mem}_{H_2O}}{\gamma} = \frac{n^C_{H_2O}}{\gamma+3} \quad (4)$$

Assuming ideal-gas behavior for gas-domain species and taking proton activity as constant within the reduced-order scope, the equilibrium (Nernst) potentials at bulk states are:

$$E^I_A(T) = E^o_a(T) + \frac{RT}{6F} ln\left(\frac{\left(P^I_{CO_2}/P_{ref}\right)}{X^I_{CH_3OH}X^I_{H_2O}}\right) \quad (5)$$

$$E^{IV}_C(T) = E^o_c(T) + \frac{RT}{6F} ln\left(\frac{\left(P^{IV}_{O_2}/P_{ref}\right)^{3/2}}{\left(P^{IV}_{H_2O}/P_{ref}\right)^3}\right) \quad (6)$$

Here $X^s_{CH_3OH}$ ($s \in \{I,II\}$) denotes the dimensionless aqueous methanol availability defined as $X^s_{CH_3OH} \equiv a^s_{CH_3OH} \approx C^s_{CH_3OH}/C_{ref}$. The liquid-water activity is approximated as $a^s_{H_2O} \approx 1$ unless otherwise specified.

Therefore, the reversible cell voltage at bulk states is

$$E_{rev} \equiv E^{IV}_C - E^I_A \quad (7)$$

Partial pressures are obtained from mole fractions:

$$p^s_k = X^s_k P^s \ (k \in \{CO_2, H_2O(v), O_2\}) \quad (8)$$

2.3 Voltage model and no-double-counting convention

The working cell voltage is expressed as the reversible (equilibrium) voltage evaluated at bulk/channel reference states minus additive loss terms:

$$V_{cell} = V_{rev} - \eta_{total} \quad (9)$$

$$\eta_{total} = \eta_{act} + \eta_{con} + \eta_{ohm} \quad (10)$$

In this work, E_{rev} is evaluated at bulk/ channel states (I, IV), while η_{conc} accounts for the Nernst-equilibrium shift caused by transport from bulk to reaction interfaces (I→II and IV→III), avoiding double counting of depletion effects.

2.4 Through-plane transport closures

Transport through porous layers is represented by linear through-plane diffusion relations. The reaction-side mole fractions are expressed as functions of current density i. On the anode side, X_{CH_3OH} and X_{H_2O} are used as effective availability variables consistent with the implementation (i.e., normalized liquid-phase composition/activity proxies), rather than gas-phase mole fractions. Accordingly, Eqs. (11) – (13) serve as lumped through-plane transport closures within the ROM framework.

Anode-side (state II):

$$X^{II}_{CH_3OH} = X^I_{CH_3OH} - \frac{RTi}{6FP^A D_{CH_3OH,H_2O}} t^A \quad (11)$$

$$X^{II}_{H_2O} = X^I_{H_2O} - \frac{(\gamma+1)iRT}{6FP^A D_{CH_3OH,H_2O}} t^A \quad (12)$$

$$X^{II}_{CO_2} = X^I_{CO_2} + \frac{iRT}{6FP^A D_{CH_3OH,H_2O}} t^A \quad (13)$$

Cathode-side (state III):

$$X_{O_2}^{III} = X_{O_2}^{IV} - \frac{RTi}{4FP^c D_{O_2,H_2O}} t^C \quad (14)$$

$$X_{H_2O}^{III} = X_{H_2O}^{IV} + \frac{RTi(\gamma+3)t^C}{6FP^C D_{O_2,H_2O}} \quad (15)$$

Water crossover across the membrane significantly influences both reactant dilution at the anode and water balance at the cathode. Accordingly, the model defines the net water flux through the PEM as a combination of two opposing mechanisms the forward electro-osmotic drag driven by proton flow, and the backward diffusion triggered by the through-plane water-content gradient yielding the following equation:

$$n_{H_2O}^M = c_{drag}^{SAT} \frac{\lambda}{22} \frac{i}{F} - \frac{\rho_{dry,Nafion}}{M_{Nafion}} D_{H_2O,Nafion} \frac{d\lambda}{dx} \quad (16)$$

In Eqs. (11) – (15), D_{CH_3OH,H_2O} and D_{O_2,H_2O} serve as lumped closure parameters that characterize the effective through-plane mass-transport resistance across the anode and cathode porous layers, respectively. These effective diffusivities aggregate complex microstructural effects such as porosity and tortuosity along with any unresolved multiphase or flooding penalties into a single, computationally efficient parameter. This approach maintains consistency with the underlying implementation. Furthermore, the dimensionless parameter γ represents the net membrane water-transport ratio, accounting for the coupled effects of electro-osmotic drag and back diffusion. In this framework, γ is determined implicitly through membrane water-balance relations and the drag coefficient (c_{drag}) (Eps. 16), following the established computational regimes of the original model.

2.5 Overpotential

2.5.1 Concentration loss

Using the half-cell Nernst forms, concentration losses are defined as the equilibrium-potential drops associated with transport from the bulk/channel states to the reaction-side states. Accordingly, the total concentration loss is decomposed as:

$$\eta_{con} = \eta_{con,a} + \eta_{con,c} \quad (17)$$

Anode Nernst shift (I→II): The anode concentration loss is expressed as the Nernst-equilibrium shift between states I (bulk) and II (reaction-side).

$$\eta_{con,a} = \frac{RT}{6F} ln \left[\frac{X_{CH_3OH}^{II} X_{H_2O}^{I} X_{CO_2}^{II}}{X_{CO_2}^{I} X_{CH_3OH}^{I} X_{H_2O}^{II}} \right] \quad (18)$$

Cathode Nernst drop (IV→III): Similarly, the cathode concentration loss is written as the Nernst drop from the bulk cathode state IV to the reaction-side state III.

$$\eta_{con,c} = \frac{RT}{6F} ln \left[\frac{X_{O_2}^{IV\frac{3}{2}} X_{H_2O}^{III\,3}}{X_{O_2}^{III\frac{3}{2}} X_{H_2O}^{IV\,3}} \right] \quad (19)$$

All Nernst-shift terms are expressed on a 6-electron cell-reaction basis for consistency with the overall DMFC stoichiometry; therefore, a common factor *RT/6F* is used in Eqs. (18) – (19).

These definitions are consistent with the model implementation, where E_{rev} is evaluated at the bulk/channel reference states, and any transport-induced equilibrium shifts are explicitly assigned to the concentration overpotential (η_{con}). This approach adheres to the adopted no-double-counting convention, ensuring a rigorous separation between thermodynamic potentials and transport losses. To enhance numerical robustness, the anode concentration loss is constrained to be non-negative, i.e., $\eta_{con,a} \leftarrow \max(\eta_{con,a}, 0)$, mirroring the treatment in the computational code to prevent unphysical values during iterative convergence.

2.5.2 Activation loss

Activation polarization is represented by the activation overpotential, which is decomposed into anode and cathode contributions:

$$\eta_{act} = \eta_{act,a} + \eta_{act,c} \quad (20)$$

Following the Butler–Volmer framework, the electrode kinetics is treated using the same Tafel approximation under practical polarization conditions. The resulting closed-form activation losses at the anode and cathode are written as:

$$\eta_{act,a} = \frac{RT}{a_a F} \left[ln\left(\frac{i_a}{i_{o,ref}}\right) - ln\left(X_{CH_3OH}^{II}\right) \right] \quad (21)$$

$$\eta_{act,c} = \frac{RT}{a_c F} \left[ln\left(\frac{i_c}{i_{o,ref}}\right) - ln\left(\frac{P^c X_{O_2}^{III}}{P_{ref}}\right) \right] \quad (22)$$

Here P_{ref} is a reference pressure used to render the logarithm dimensionless, i_a and i_c denote the anode and cathode current densities (A·m^{-2}); under steady-state operation of a single-cell model, neglecting crossover-induced parasitic currents i_a=i_c=i. The parameter $i_{0,ref}$ is the reference exchange current density (A·m^{-2}), while a_a and a_c are the charge-transfer coefficients.

2.5.3 Ohmic polarization

The ohmic loss is computed from the area-specific membrane resistance:

$$\eta_{ohm} = iR^{mem} = i \int_0^{t^M} \frac{dx}{\sigma_m(T,x)} \quad (23)$$

$\sigma_m(T,x)$ is the proton conductivity, modeled by the standard Nafion correlation [16]:

$$\sigma(T,x) = (0.5193\lambda - 0.326) exp\left[1268\left(\frac{1}{303} - \frac{1}{T}\right)\right] \quad (24)$$

To establish the boundary conditions for the membrane water content (λ), the local water activities ($a_w = P_w/P_{SAT}$) are evaluated at both the anode-membrane and cathode-membrane interfaces using the standard $\lambda(a_w)$ correlation. Subsequently, the derived spatial profile, $\lambda(x)$, is substituted into Eqs. (23) and (24) to calculate the ohmic overpotential (η_{ohm})

2.6 Lumped thermal submodel

To estimate transient/steady temperature at selected operating points, a lumped thermal balance is evaluated outside the electrochemical loop; thus, temperature does not feed back into kinetic/transport parameters in the present work. The heat-generation rate is linked to the total voltage deficit:

$$Q_g(i) = A_{act} i (E_{th} - V_{cell}) \quad (25)$$

Heat rejection to the ambient is modeled by a convective term, yielding the lumped energy balance [17]:

$$mc_p \frac{dT}{dt} = Q_g(i) - hA_s(T - T_m) \quad (26)$$

For constant current density i and constant h, the solution is:

$$T(t) = T_m + \frac{A_{act} i (E_{th} - V_{cell})}{hA_s}\left(1 - e^{\frac{-t}{\tau}}\right) \quad (27)$$

Accordingly, the thermal time constant is defined as:

$$\tau = \frac{mc_p}{hA_s} \quad (28)$$

The lumped thermal model is used for load-dependent screening and neglects any additional heat release associated with methanol crossover.

2.7 Quasi-steady evaluation

The current density i is used as the control variable. For each prescribed i, internal transport and electrochemical processes are assumed quasi-steady, so V, P, and loss components are single-valued functions of i. The operating domain $[i_{min}, i_{max}]$ was discretized into $\{i_1, \ldots. i_n\}$, i_k. Each point i_k represents an independent steady operating state, allowing the ROM to be evaluated pointwise without time-marching iterations. This discretization enables clear assessment of how activation, ohmic, and concentration losses evolve across low-, mid-, and high-load regimes.

Figure 2 summarizes the quasi-steady evaluation procedure. After specifying the operating conditions and material parameters, the limiting current density i_L is determined from methanol and oxygen transport constraints. The polarization characteristics are then obtained by sweeping the current density from $i=i_{min}$ up to approximately i_L, where $i_{min} > 0$ is a small positive value introduced to avoid logarithmic singularities, with early termination enforced when physical feasibility conditions are violated. For any given current density, the net water-transfer coefficient (γ) is determined by solving the implicit water-conservation equations, which actively balance electro-osmotic drag against back diffusion. Subsequently, the model calculates the kinetic, resistive, and mass-transport voltage penalties to establish the final cell potential and power output. The maximum power point (i_{Pmax}, P_{max}) is subsequently identified and used to estimate the maximum heat generation rate Q_{max}. Subsequently, a lumped thermal model is integrated in time to predict the transient temperature response under selected fractions of Q_{max}. As a numerical safeguard, early termination is applied if any feasibility constraint is violated, e.g., $V_{cell} < 0.1$ V or any required gas-domain mole fraction/partial pressure becomes non-positive.

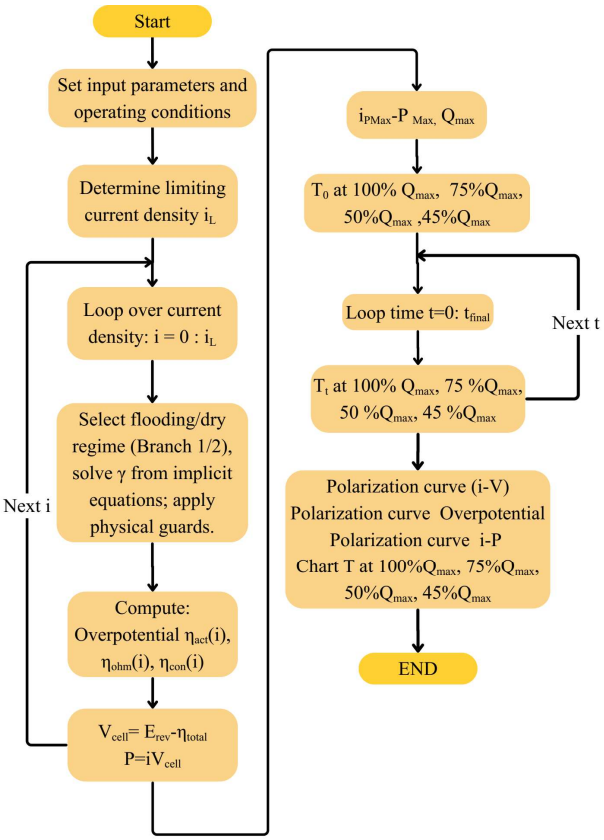

Fig. 2. Flowchart of the proposed quasi-steady DMFC model.

2.8 Validation and error metrics

The model was validated against the experimental polarization data reported by Xu and Faghri [18]. The experimental i–V points were digitized from the published figure and compared with the simulated voltages matching nominal conditions (P = 1.013×10^5 Pa, T = 298 K), and anode methanol feed concentrations of 2 M and 3 M (Figures 3 and 4). Error metrics were evaluated over the common current-density window of 200–2500 A m^{-2} using N = 24 data points. The mean absolute error (MAE) and root-mean-square error (RMSE) were calculated using Eqs. (29) and (30), respectively:

$$MAE = \frac{1}{N}\sum_{k=1}^{N}\left|V_{sim,k} - V_{exp,k}\right| \quad (29)$$

$$RMSE = \sqrt{\frac{1}{N}\sum_{k=1}^{N}\left(V_{sim,k} - V_{exp,k}\right)^2} \quad (30)$$

where $V_{sim,k}$ and $V_{exp,k}$ are the simulated and digitized experimental voltages at the k common current-density point, and N is the number of data points.

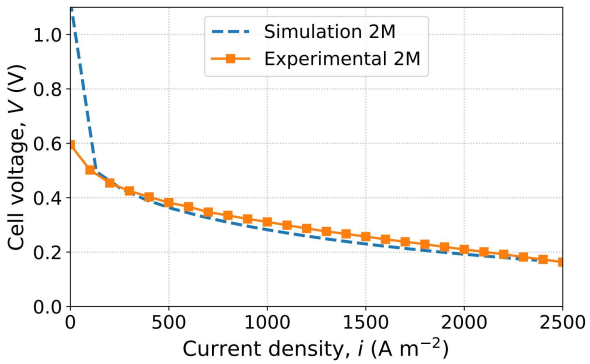

Fig. 3. DMFC modelling results compared to experimental data from *C. Xu [18]* at $p^a = p^c = 1.013 \times 10^5$ Pa, $T_m = 298$ K, 2 M methanol.

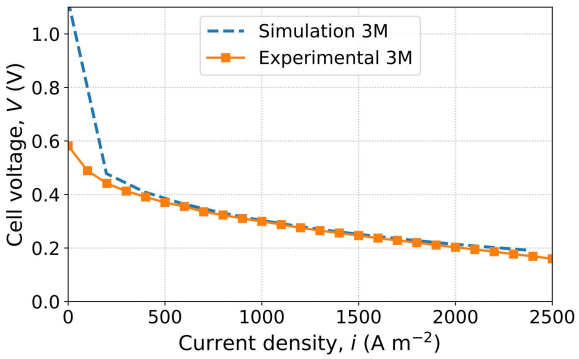

Fig. 4. DMFC modelling results compared to experimental data from *C. Xu [18]* at $p^a = p^c = 1.013 \times 10^5$ Pa, $T_m = 298$ K, 3 M methanol.

As summarized in Table 1, the model shows good agreement with the digitized polarization data, with MAE ≤ 0.0192 V and RMSE ≤ 0.021 V, indicating close agreement over 200–2500 A m^{-2} for both methanol concentrations. The validation was performed under the nominal conditions reported by Xu and Faghri [18], whereas the subsequent case study uses the baseline conditions listed in Table 2. No formal multi-parameter calibration was conducted; literature-based and assumed parameters were kept fixed, and model agreement was assessed a posteriori using MAE and RMSE. Therefore, the validation is interpreted as a consistency check of the ROM rather than a full parameter-identification exercise.

Table 1. Summary of validation errors for different methanol concentrations.

Methanol concentration	MAE (V)	RMSE (V)
2 M	0.0192	0.021
3 M	0.0123	0.015

3. RESULTS AND DISCUSSION

After validating the ROM against published polarization data (Section 2.8), we conduct a separate case study under a user-defined baseline condition to examine loss budgets, power characteristics, and thermally constrained operating points, with parameters and operating conditions summarized in Table 2.

3.1 Polarization behavior (i–V)

Figure 5 shows the simulated polarization curve at 50 °C. The cell voltage decreases rapidly in the low-current region and reaches approximately 0.36 V at i = 200 Am^{-2}. The decay becomes more gradual at intermediate current densities, followed by an accelerated drop for i ≥ 1500 A m^{-2}, approaching 0.1 V near the upper end of the simulated range (2038 Am^{-2}). This trend is consistent with the transition from activation-dominated behavior at low current densities to behavior increasingly affected by transport-induced depletion at high current densities. The voltage drop is interpreted through effective activation, ohmic, and bulk-to-interface concentration-loss terms. Since methanol-crossover-induced mixed potentials and two-phase effects such as liquid-water flooding and CO_2 bubble transport are not explicitly resolved, the high-current branch should be interpreted within the reduced-order single-phase scope. This motivates the subsequent loss-budget analysis across low-, intermediate-, and high-load regimes.

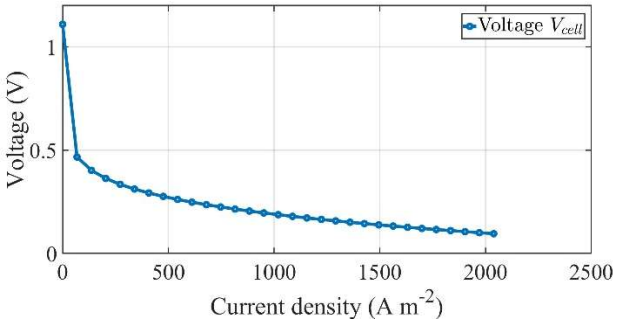

Fig. 5. Polarization curve (i-V) predicted by the passive DMFC model.

3.2 Voltage Loss Analysis

Figure 6 shows the variation of the total activation loss with current density. The activation loss increases sharply at low current density and continues to rise over the entire investigated range, confirming that charge-transfer kinetics remain the dominant source of voltage penalty for this DMFC under the present conditions. In the low-current regime, the curve exhibits a steep slope because Butler–Volmer kinetics are strongly nonlinear: when i is small, a finite activation overpotential is required to overcome the reaction barrier, such that a modest increase in i produces a pronounced increase in η_{act}. The predominance of activation loss is physically consistent with the sluggish methanol oxidation kinetics typically observed in DMFCs, where the anode reaction involves multiple intermediate steps and generally requires substantially higher catalyst loading than hydrogen oxidation in conventional PEM fuel cells. Therefore, the large activation penalty predicted by the ROM should be interpreted as an effective total kinetic contribution rather than as a fully resolved separation of anode and cathode reaction pathways.

Table 2. Model parameters and operating conditions used in the DMFC simulations

Property (including unit)	Value	Reference
Theoretical (LHV-based) voltage, E_{th}	1.18	[1]
Standard pressure, P_{ref} (Pa)	1.013×10^5	[19]
Universal gas constant, R (J mol^{-1} K^{-1})	8.314	
Faraday constant, F (C mol^{-1})	96485	
Baseline electrochemical temperature, T (K)	323	
Ambient temperature, T_m (K)	298	Assumed
Anode pressure, P_A (Pa)	1.013×10^5	Assumed
Cathode pressure, P_C (Pa)	1.013×10^5	
Anode porous-layer thickness, t^A (µm)	400	
Cathode porous-layer thickness, t^C (µm)	400	
Membrane thickness, t^M (µm)	175	Nafion 117
Active area, A_{act} (m^2)	1×10^{-3}	
Heat-transfer area, A_s (m^2)	$2 \times A_{act}$	
Convective coefficient, h (W m^{-2} K^{-1})	10	Adopted from [20]
Water saturation pressure, P_{sat} (Pa)		Computed from [19]
Effective cathode-side diffusivity parameter, $D_{O2,H2O}$ (m^2 s^{-1})	2.95×10^{-6}	[19]
Effective anode-side diffusivity parameter, $D_{CH3OH,H2O}$ (m^2 s^{-1})	6.7×10^{-6}	Adopted from [16]
Water-in-Nafion diffusivity, D_{WN} (m^2 s^{-1})	1.3413×10^{-10} exp [2416(1/303 − 1/T)]	[16]
Reference exchange current density, $i_{0,ref}$ (A m^{-2})	1	Assumed
Water drag coefficient, C_{drag}	2.5	[16]
Membrane density, ρ_N (kg m-3)	1970	Nafion 117
Equivalent-weight proxy in code, E_W (kg mol^{-1})	1.0	[19]
Anode inlet CH_3OH concentrations (M)	1	
O2 fraction in air, $y_{O2,air}$	0.21	
Thermal lumped mass, m (kg)	0.045	Assumed
Specific heat, c_p (J kg^{-1} K^{-1})	900	Assumed
Reference temperature threshold, T_{ref} (K)	363	[21]

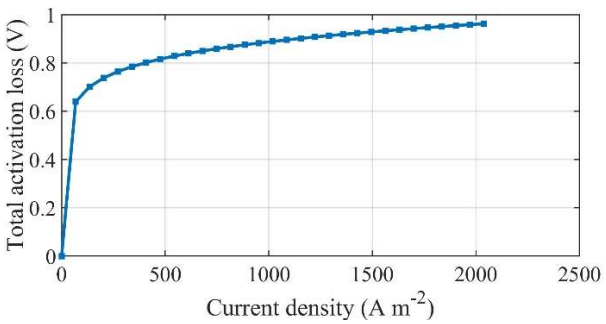

Fig. 6. Activation loss versus current density at 323 K.

Quantitatively, for i < 100 A m^{-2}, the activation loss rises rapidly from near zero to approximately 0.45–0.5 V. In the intermediate range (100–1500 Am^{-2}), the activation loss continues to increase but more gradually, from about 0.74 V to roughly 0.93 V, consistent with the logarithmic (Tafel-type) dependence implied by the adopted kinetic approximation. At higher current density, the incremental growth further weakens and the activation loss approaches 0.94–0.95 V at i = 2000–2038 Am^{-2}. This behavior indicates diminishing marginal activation penalties at large loads, such that additional voltage decay at elevated current density is increasingly attributable to transport-induced depletion and the accumulation of other loss mechanisms rather than to a continued steep rise in kinetic polarization alone.

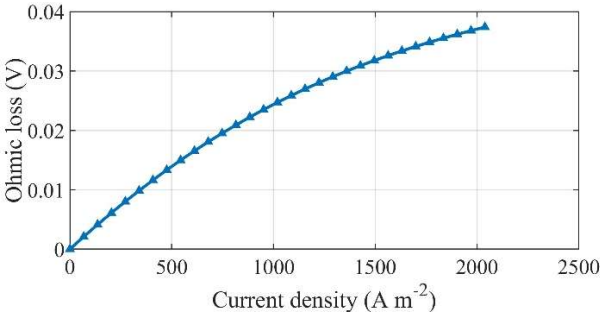

Fig. 7. Ohmic loss versus current density at 323 K.

Figure 7 presents the variation of the ohmic loss with current density. The ohmic loss increases smoothly from 0 V at open circuit to about 0.0133–0.015 V at i = 500 Am^{-2} and reaches approximately 0.0235–0.0318 V at i = 1000–1500 Am^{-2}. At higher current densities (1500–2100 Am^{-2}), η_{ohm} continues to increase from roughly 0.0318 V to a maximum near 0.0376 V.

The curve shows a mild reduction in slope at high current density, indicating weak nonlinearity consistent with hydration-dependent membrane ionic conductivity embedded in the Nafion conductivity correlation. Overall, the ohmic contribution remains small compared with the activation loss, implying that under the present case-study condition the voltage decay is not primarily governed by resistive limitations. Accordingly, the predicted ohmic loss is best interpreted as an effective membrane/electrolyte ionic contribution associated with proton transport through the polymer electrolyte membrane, rather than as a complete in situ cell resistance. Additional ohmic contributions associated with contact interfaces, electronic pathways, and assembly-dependent resistances may also exist in practical cells, although they are not explicitly separated in the present ROM. Accordingly, membrane hydration, membrane thickness, ionic conductivity, and interfacial contact resistance remain relevant sensitivity parameters for future model refinement.

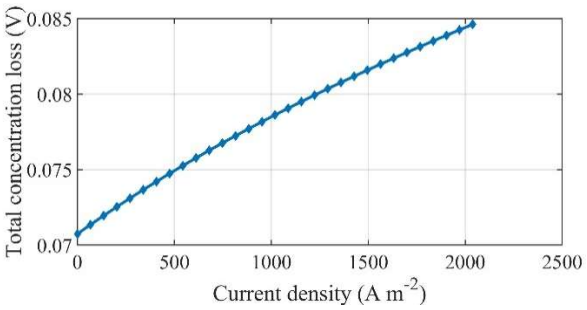

Fig. 8. Concentration loss versus current density at 323 K.

Figure 8 shows the variation of the total concentration loss with current density under the simulated condition. The concentration loss, defined here as the transport-induced Nernst shift between bulk/channel and reaction-side states under the adopted no-double-counting convention, remains comparatively small but increases monotonically over the full range. Specifically, η_{con} increases from approximately 0.07 V at low current density to about 0.0846 V at the highest current density.

In the low-to-intermediate regime, the increase is slow and nearly linear, indicating that interface depletion remains limited and that transport constraints are not yet severe. Although moderate in magnitude relative to η_{act}, this concentration component contributes to the accelerated decline of the cell voltage in the upper operating region predicted by the ROM.

This trend reflects a gradual increase in bulk-to-interface reactant depletion as the load increases. The moderate and nearly monotonic rise of ηcon suggests that severe limiting-current behavior is not reached within the simulated range. Accordingly, ηcon is interpreted as an effective single-phase Nernst-shift contribution in the present ROM, while methanol crossover, two-phase transport, local starvation, and channel-wise concentration gradients remain relevant directions for future refinement

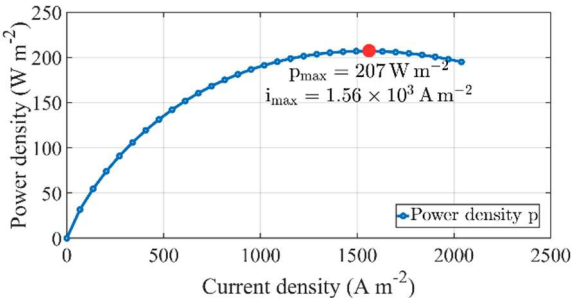

Fig. 9. Power density response of the passive DMFC under the baseline operating condition.

Figure 9 shows the simulated power density as a function of current density for the passive DMFC. The power curve exhibits the expected rise–peak–decline behavior, reflecting the competition between increasing current and the concurrent voltage drop caused by cumulative overpotentials. This behavior can be interpreted from the relation $P = iV$. At low and intermediate current densities, the incremental gain associated with increasing current density remains larger than the voltage penalty caused by cumulative activation, ohmic, and concentration losses; therefore, the power density continues to increase. Near Pmax, these two competing effects become balanced, such that the additional current no longer provides a net power gain sufficient to compensate for the loss-induced voltage decrease. Beyond this point, the voltage drop becomes dominant, and the power density decreases even though the current density continues to increase. At low current density ($i \leq$ 500 Am^{-2}), the power density increases rapidly from near zero to approximately 131.33–142.1 Wm^{-2} because the cell voltage remains relatively high while resistive and transport penalties are still limited.

In the intermediate region (1359 –1427.1 Am^{-2}), the rate of power increase decreases: the power density reaches roughly 205.5 Wm^{-2} at i = 1359 Am^{-2} and approaches about 206.3 Wm^{-2} at i = 1427.1 Am^{-2}, indicating that growing activation, ohmic, and concentration losses progressively offset the benefit of increasing current. The maximum power density is 207 Wm^{-2} at i = 1563 Am^{-2}, where the corresponding cell voltage is about 0.1324 V. Beyond this point, the power density declines to around 195-202.7 W m^{-2} at i = 1834.8–2038.7 Am^{-2}, as the accelerated voltage drop at high current density outweighs further increases in current. This trend is consistent with the onset of stronger transport-induced depletion at elevated loads. Thus, P_{max} represents the electrical maximum under the present conditions, whereas a slightly lower-load region may offer a more balanced compromise among power output, voltage efficiency, reactant demand, and thermal safety.

Combining the thermal results (Figure 10) with the current–power–reactant molar-flux relationship in Figure 11 reveals a clear trade-off between maximizing instantaneous electrical power and achieving a thermally and supply-feasible operating regime. Two representative points are considered: the peak-power point P_{max} and a mid-load point near 75% of peak power.

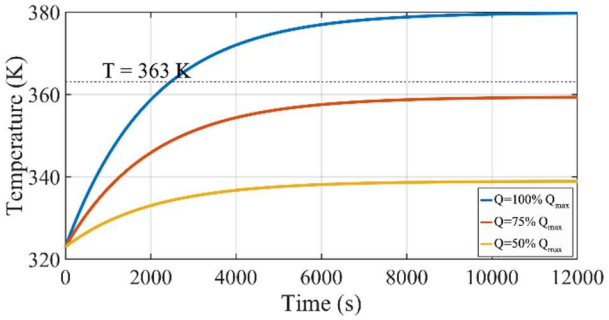

Fig. 10. Lumped transient temperature response.

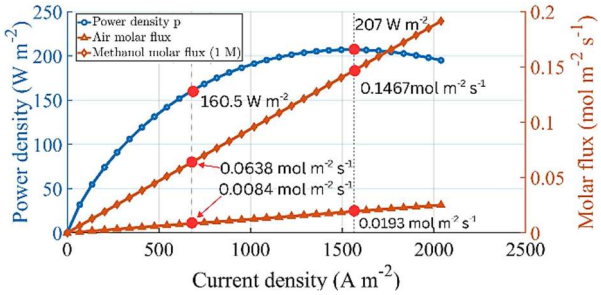

Fig. 11. Power density and reactant molar-flux requirements versus current density.

At P_{max}, the cell delivers P = 207 Wm^{-2} at i = 1563 Am^{-2} with molar fluxes of N_{air} = 0.0193 molm^{-2}s^{-1} and N_{CH3OH} = 0.14673 molm^{-2}s^{-1}. The strong increase in reactant molar fluxes with i is consistent with the stoichiometric scaling adopted in the model. However, the substantial voltage drop at high current density implies that the incremental power gain becomes increasingly disproportionate to the additional supply demand and the heightened sensitivity to transport limitations.

In contrast, at 75% of Q_{max}, the cell produces P = 160.48 Wm^{-2} at i = 679.57 Am^{-2}, with N_{air} = 0.0084 molm^{-2}s^{-1} and N_{CH3OH} = 0.0638 molm^{-2}s^{-1}. Relative to Q_{max}, the current density decreases by 2.3 times and the methanol molar flux decreases by 2.3 times (air flux by 2.3 times), whereas power decreases by only 1.3 times, indicating that the mid-load regime retains a substantial fraction of power with markedly lower supply demand due to a comparatively higher operating voltage. This comparison indicates that the peak-power point is not necessarily the most favorable operating point when system-level constraints are considered. Higher power density is achieved at lower cell voltage and requires larger reactant supply, whereas the 75% Q_{max} point retains a substantial fraction of the electrical output with lower molar-flux demand and improved voltage utilization. This is consistent with fuel-cell system design practice, where operating-point selection involves a compromise among power density, efficiency, fuel supply, thermal management, and operating duration rather than maximum instantaneous power alone.

Moreover, the lumped thermal model (Figure 10) estimates that operation around 75% of Q_{max} can maintain a steady temperature of 86.0 °C (359.15 K) which is below 363 K under passive heat rejection [21], whereas sustained operation near Q_{max} tends to exceed this threshold without active thermal management. Therefore, when electrical output, thermal safety, and reactant supply constraints are considered together, operation around 75% of peak power may be preferred, while operation close to Q_{max} requires improved heat rejection and mass-transport management to mitigate overheating risk and operating sensitivity.

At *75% Q_{max}*, the model predicts V = 0.2361 V at i = 679.57 Am^{-2} (P = 160.48 W m^{-2}) with an operating efficiency of approximately 20%. Here, the operating efficiency is defined as the ratio of useful electrical power to the chemical energy input of methanol based on the adopted heating value, i.e., $\eta = P/(n_{CH3OH}\,\Delta H)$. The loss budget at this point is dominated by activation polarization (η_{act} = 0.8495 V), while the concentration loss remains moderate (η_{con} = 0.0763 V) and the ohmic contribution is comparatively small (η_{ohm} = 0.0181 V), yielding a total voltage deficit of η_{total} = 0.9439 V. Consistent with this deficit, the dissipated power at the same operating point (P_{loss} = 0.641 W) exceeds the delivered electrical power (P_{use} = 0.160 W), indicating that kinetic improvements and heat rejection capability remain critical even under mid-load operation.

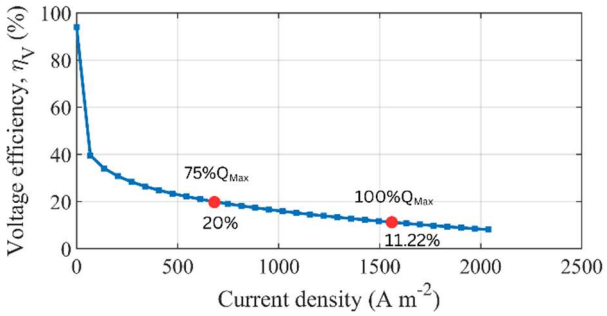

Fig. 12. Voltage efficiency at the selected mid-load and peak-load operating points.

Figure 12 adds a voltage-efficiency perspective to the operating-point selection, with η_v=V/E_{th} . The selected 75% Q_{max} condition retains η_v=20.0% compared with only 11.22% near 100% Q_{max}. The additional power obtained near the peak-load condition is therefore accompanied by a disproportionate voltage-efficiency penalty and higher reactant demand. This trend is consistent with transport-resolved DMFC studies, where high-current operation becomes increasingly sensitive to reactant depletion, water accumulation, CO_2 removal, and oxygen-access limitations [6], [10], [22].

Consequently, for the present passive-DMFC screening case, the 75% Q_{max} point provides a more balanced operating regime by combining lower methanol/air demand, safer passive thermal operation, and higher voltage efficiency than operation near Q_{max}.

The dominance of activation polarization is consistent with previous DMFC studies that identify sluggish methanol oxidation kinetics as a major voltage-loss source [2], [5]. The increase in concentration loss at high current also agrees qualitatively with transport-resolved studies, where reactant depletion, water accumulation, CO_2 transport, and oxygen-access limitations become more important [6], [10], [22]. Accordingly, the model response is mainly sensitive to $i_{0,ref}$, effective diffusivities, membrane resistance, and the heat-transfer coefficient h. Because these effects are treated through effective single-phase closures, high-current predictions should be interpreted as reduced-order estimates rather than fully resolved flooding, crossover, or limiting-current behavior.

4. CONCLUSION

This work introduces a computationally efficient, 1D physics-based reduced-order model (ROM) tailored specifically for passive direct methanol fuel cells (DMFCs). The framework is formulated to quickly evaluate power and polarization responses, alongside providing a rigorous breakdown of internal voltage penalties. The reversible voltage was evaluated at bulk/channel reference states, while bulk-to-interface Nernst shifts were consistently assigned to the concentration loss using a strict no-double-counting convention. The ROM was validated against published polarization data over 200 – 2500 Am^{-2}, achieving MAE/RMSE values of 0.0192 / 0.021 V (2.0 M) and 0.0123 / 0.015 V (3.0 M).

In a 50 °C case study, the model successfully reproduced a bell-shaped power curve with a predicted peak power density of 207 Wm^{-2} near 1563 Am^{-2}. Loss budgeting revealed that activation polarization dominates across most of the operating range, whereas ohmic losses remain minimal and concentration losses increase moderately with load. Furthermore, combined electrical–thermal screening suggests that operating at approximately 75% of provides an optimal trade-off between power output, efficiency (20%), and thermal safety under passive heat rejection. Ultimately, the primary contribution of this work lies in this internally consistent voltage-loss budgeting and thermal-screening framework, moving beyond the mere application of a 1D reduced-order formulation. These features make the ROM a highly effective front-end screening tool for practical passive-DMFC power modules such as portable electronics, remote sensor nodes, and backup power supplies where rapid design iteration and thermally safe operation are essential.

Nevertheless, these conclusions must be interpreted within the model's reduced-order scope. The current formulation relies on effective single-phase transport closures; it does not explicitly resolve methanol crossover or crossover-induced mixed potentials, nor does it account for liquid-water flooding, CO_2 bubble transport, or two-way electrochemical–thermal feedback. Additionally, as validation is presently limited to digitized polarization data at two methanol concentrations, broader validation across varied temperatures, cell designs, and operating regimes is necessary. Therefore, future work will focus on extending the framework by incorporating crossover and multiphase corrections, coupling temperature feedback to kinetic and transport parameters, conducting comprehensive sensitivity/uncertainty analyses, and validating the model against a wider array of experimental datasets, particularly under high-current and passive thermal-management conditions.

NOMENCLATURE

a_a	=	Anode charge-transfer coefficient
a_c	=	Cathode charge-transfer coefficient
a_k^s	=	Activity of species k at state s
a_{H2O}^I	=	Liquid-water activity at anode bulk state I
a_w	=	Water activity at membrane interface
A_{act}	=	Electrochemically active area (m^2)
A_s	=	External heat-transfer area (m^2)
c_p	=	Lumped specific heat capacity ($J \cdot kg^{-1} \cdot K^{-1}$)
c_{drag}	=	Electro-osmotic drag coefficient
C_{CH3OH}^s	=	Methanol concentration at state s ($mol \cdot m^{-3}$)
C_{ref}	=	Reference concentration for activity normalization ($mol \cdot m^{-3}$)
$D_{CH3OH,H2O}$	=	Effective CH_3OH diffusivity in anode porous layer (GDL) ($m^2 \cdot s^{-1}$)
$D_{O2,H2O}$	=	Effective O_2 diffusivity in cathode porous layer ($m^2 \cdot s^{-1}$)
$E_a^0(T)$	=	Anode standard equilibrium potential at temperature T (V)
$E_c^0(T)$	=	Cathode standard equilibrium potential at temperature T (V)
$E_A^I(T)$	=	Anode equilibrium (Nernst) potential at bulk state I (V)
$E_C^{IV}(T)$	=	Cathode equilibrium (Nernst) potential at bulk state IV (V)
E_{rev}	=	Reversible cell voltage evaluated at bulk states (V)
F	=	Faraday constant ($C \cdot mol^{-1}$)
h	=	Convective heat-transfer coefficient ($W \cdot m^{-2} \cdot K^{-1}$)
i	=	Operating current density ($A \cdot m^{-2}$)
i_a	=	Current density at the anode ($A \cdot m^{-2}$)
i_c	=	Current density at the cathode ($A \cdot m^{-2}$)
i_L	=	Mass-transport limiting current density ($A \cdot m^{-2}$)

$i_{0,ref}$	=	Reference exchange current density ($A \cdot m^{-2}$)
M	=	Lumped mass in thermal model (kg)
n_k	=	Molar flux (or molar consumption/production rate per area) of species *k* ($mol \cdot m^{-2} \cdot s^{-1}$)
P_s	=	Total pressure at state *s* (Pa)
P_{ref}	=	Reference pressure for nondimensionalization (Pa)
p_k^s	=	Partial pressure of gaseous species k at state s (Pa)
P	=	Output power per unit area ($W \cdot m^{-2}$)
P_{max}	=	Peak power density ($W \cdot m^{-2}$)
i_{Pmax}	=	Current density corresponding to peak power ($A \cdot m^{-2}$)
$Q_g(i)$	=	Heat-generation rate (W)
Q_{max}	=	Maximum heat-generation rate (W)
R	=	Universal gas constant ($J \cdot mol^{-1} \cdot K^{-1}$)
R_{mem}	=	Membrane area-specific resistance ($\Omega \cdot m^2$)
t^A	=	Anode porous-layer thickness (m)
t^C	=	Cathode porous-layer thickness (m)
t^M	=	Thickness of the electrolyte membrane (m)
T	=	Operating temperature of the cell (K)
T_m	=	Ambient temperature (K)
V_{cell}	=	Working cell voltage (V)
X_k^s	=	Mole fraction of gaseous species k at state s
X_{CH3OH}; X_{H2O}	=	Aqueous availability proxies (normalized activity/concentration), not gas-phase mole fractions.
γ	=	Net membrane water-transport ratio
η_{total}	=	Total voltage loss (V)
η_{act}	=	Activation loss (V)
η_{con}	=	Concentration (Nernst-shift) loss (V)
η_{ohm}	=	Ohmic loss (V)
$\eta_{act,a}$; $\eta_{act,c}$	=	Anode/cathode activation losses (V)
$\eta_{con,a}$; $\eta_{con,c}$	=	Anode/cathode concentration losses (V)
λ	=	Membrane water content (mol H_2O per mol SO_3^-)
$\sigma^m(T,x)$	=	Membrane proton conductivity ($S \cdot m^{-1}$)
τ	=	Thermal time constant, (s)
a	=	Anode
c	=	Cathode
act	=	Activation
con	=	Concentration
ohm	=	Ohmic
k	=	Species index
ref	=	Reference value
m	=	Ambient (in T_m)
max	=	Maximum
0	=	Standard-state (in E^0)
A	=	Anode-side quantity/condition
C	=	Cathode-side quantity/condition
M	=	Membrane
I, II, III, IV	=	Through-plane states as defined in Fig. 1

ACKNOWLEDGEMENT

The authors gratefully acknowledge the institutional support and resources provided by the Faculty of Energy Engineering and Transport at Ho Chi Minh University of Technology and Engineering (HCM-UTE).

DECLARATIONS

Author Contributions

The conceptualization of the research and the design of the methodology were jointly carried out by Thanh-Tuan Pham and Phuoc Thanh Nguyen. Both researchers participated in data processing, formal analysis, and the drafting of the manuscript. Furthermore, they thoroughly reviewed and refined the final document, mutually approving its submission for publication.

Conflicts of Interest

The authors report no relevant financial or non-financial competing interests to disclose.

REFERENCES

[1] Liu, J.G., Zhao, T.S., Chen, R., and Wong, C.W., 2005. The effect of methanol concentration on the performance of a passive DMFC. *Electrochemistry Communications* 7(3): 288–294. doi:10.1016/j.elecom.2005.01.011.

[2] Ko, J., Chippar, P., and Ju, H., 2010. A one-dimensional, two-phase model for direct methanol fuel cells – Part I: Model development and parametric study. *Energy* 35(5): 2149–2159. doi:10.1016/j.energy.2010.01.034.

[3] Karaoglan, M.U., Ince, A., Glüsen, A., Colpan, C.O., Müller, M., and Stolten, D. 2020. Comparison of single-cell testing, short-stack testing and mathematical modeling methods for a direct methanol fuel cell. *International Journal of Hydrogen Energy* 45: 35095–35107. doi:10.1016/j.ijhydene.2020.02.107.

[4] Oliveira, V.B., Rangel, C.M., and Pinto, A.M.F.R., 2011. One-dimensional and non-isothermal model for a passive DMFC. *Journal of Power Sources* 196: 8973–8982. doi:10.1016/j.jpowsour.2011.01.094.

[5] Mallick, R.K., Thombre, S.B., and Kothekar, K.P. 2018. An integral mathematical model of liquid feed passive DMFCs with non-isothermal effects and charge conservation phenomenon. *Journal of*

Cleaner Production 182: 654–671. doi:10.1016/j.jclepro.2018.01.177.

[6] Zago, M., Casalegno, A., Santoro, C., and Marchesi, R., 2012. Water transport and flooding in DMFC: Experimental and modeling analyses. *Journal of Power Sources* 217: 381–391. doi:10.1016/j.jpowsour.2012.06.022.

[7] Shrivastava, N.K., Thombre, S.B., and Mallick, R.K., 2014. Effect of diffusion layer compression on passive DMFC performance. *Electrochimica Acta* 149: 167–175. doi:10.1016/j.electacta.2014.10.080.

[8] Shu, Q.-z., Xia, Z.-x., Wei, W., Xu, X.-l., Wang, S.-l., Zhao, H., and Sun, G.-q., 2021. A novel gas diffusion layer and its application to direct methanol fuel cells. *New Carbon Materials* 36: 409–419. doi:10.1016/S1872-5805(21)60017-3.

[9] Braz, B.A., Oliveira, V.B., and Pinto, A.M.F.R., 2019. Experimental studies of the effect of cathode diffusion layer properties on a passive direct methanol fuel cell power output. *International Journal of Hydrogen Energy* 44: 19334–19343. doi:10.1016/j.ijhydene.2019.03.162.

[10] Falcão, D.S., Pereira, J.P., and Pinto, A.M.F.R., 2016. Numerical simulations of anode two-phase flow in Micro-DMFC using the volume of fluid method. *International Journal of Hydrogen Energy* 41: 19724–19730. doi:10.1016/j.ijhydene.2016.05.264.

[11] Ko, J., Lee, G., Choi, Y., Chippar, P., Kang, K., and Ju, H., 2011. Comparison of numerical simulation results with experimental current density and methanol-crossover data for direct methanol fuel cells. *Journal of Power Sources* 196(3):935–945. doi:10.1016/j.jpowsour.2010.08.102.

[12] Ko, J., Kang, K., Park, S., Kim, W.-G., Lee, S.-H., and Ju, H., 2014. Effect of design of multilayer electrodes in direct methanol fuel cells (DMFCs). *International Journal of Hydrogen Energy* 39(3): 1571–1579. doi:10.1016/j.ijhydene.2013.04.069.

[13] Wang, Y., and Sauer, D.U., 2015. Optimization of DMFC regulation based on spatial modeling. *International Journal of Hydrogen Energy* 40(35): 12023–12033. doi:10.1016/j.ijhydene.2015.06.030.

[14] Gwak, G., Lee, K., Ferekh, S., Lee, S., and Ju, H., 2015. Analyzing the effects of fluctuating methanol feed concentration in active-type direct methanol fuel cell (DMFC) systems. *International Journal of Hydrogen Energy* 40. doi:10.1016/j.ijhydene.2015.01.062.

[15] Springer, T.E., Zawodzinski, T.A., and Gottesfeld, S., 1991. Polymer electrolyte fuel cell model. *Journal of the Electrochemical Society* 138(8): 2334–2342. doi:10.1149/1.2085971.

[16] O'Hayre, R., Cha, S.-W., Colella, W., and Prinz, F.B., 2016. *Fuel Cell Fundamentals*. 3rd ed. Hoboken, NJ, USA: John Wiley & Sons. doi:10.1002/9781119191766.

[17] Winterbone, D.E., and Turan, A., 2015. *Advanced Thermodynamics for Engineers*. 2nd ed. Oxford, UK: Butterworth-Heinemann (Elsevier). doi:10.1016/C2013-0-13437-X.

[18] Xu, C., and Faghri, A., 2010. Water transport characteristics in a passive liquid-feed DMFC. *International Journal of Heat and Mass Transfer* 53(9-10): 1951–1966. doi:10.1016/j.ijheatmasstransfer.2009.12.060.

[19] Molaeimanesh, G.R., and Torabi, F. 2022., *Fuel Cell Modeling and Simulation: From Microscale to Macroscale*. Oxford, UK: Elsevier. doi:10.1016/C2020-0-02573-9.

[20] Mench, M.M. 2006. *Fuel Cell Engines*. Hoboken, NJ, USA: John Wiley & Sons, Inc. doi:10.1002/9780470209769.

[21] Jung, D.H., Lee, C.H., Kim, C.S., and Shin, D.R., 1998. Performance of a direct methanol polymer electrolyte fuel cell. *Journal of Power Sources* 71(1-2): 169–173. doi:10.1016/S0378-7753(97)02793-6.

[22] Ismail, A., Kamarudin, S.K., Daud, W.R.W., Masdar, S., and Hasran, U.A., 2018. Development of 2D multiphase non-isothermal mass transfer model for DMFC system. *Energy* 152: 263–276. doi:10.1016/j.energy.2018.03.097.